Acta Mech 195, 185–202 (2008)
DOI 10.1007/s00707-007-0550-9
Printed in The Netherlands

Acta Mechanica

Dedicated to Professor Franz Ziegler on the occasion of his 70th birthday

Failure modes and effective strength of two-phase materials determined by means of numerical limit analysis

J. Füssl[1], R. Lackner[2], J. Eberhardsteiner[1], H. A. Mang[1]

[1] Institute for Mechanics of Materials and Structures, Vienna University of Technology, Vienna, Austria
[2] Fachgebiet Computational Mechanics, Technical University of Munich, Munich, Germany

Received 2 October 2007; Accepted 21 November 2007; Published online 15 January 2008

Summary. In the most general case, composites composed of two materials, exhibiting a matrix-inclusion morphology, can be described by three phases: the matrix phase, the inclusion phase, and the interface between the inclusion and the matrix. In order to relate effective material properties to the matrix-inclusion behavior and the morphology, i.e., to the arrangement of the inclusions within the matrix phase, analytical and/or numerical schemes may be employed. Regarding effective strength properties, averaging schemes used, e.g., for upscaling elastic and viscoelastic properties are not able to capture the localized mode of material failure and do not provide information about the failure modes within the material. In this paper, the application of limit analysis to two-phase materials subjected to uniaxial/biaxial loading is proposed, giving access to the respective material strength and the corresponding failure modes. Based on a discretized form of limit analysis, different strength properties are assigned to the matrix, the inclusion, and the interface. The solution of the underlying optimization problem arising from the respective upper- and lower-bound formulation is based on second-order-cone-programming (SOCP). The presented upscaling scheme is used to illustrate the finer-scale origin of frequently observed failure and degradation scenaria in matrix-inclusion materials, highlighting the effect of strength properties, morphology, and interface degradation on the effective strength of the composite material.

1 Introduction

In order to explain and, finally, predict the strength-determining processes in composite materials, appropriate methods for relating the effective strength to its finer-scale origin are required. Depending on the microstructure of the material (regular or randomly distributed), two modes of establishing this relation (also referred to as "upscaling") may be distinguished:

- *Unit-cell approach:* if the material microstructure is characterized by the spatial variation of physical quantities which can be represented by a combination of local fluctuations at the level of the elementary cell and a drift of this elementary cell, the periodic media theory may be employed.

Correspondence: J. Füssl, Institute for Mechanics of Materials and Structures, Vienna University of Technology, Karlsplatz 13, 1040 Vienna, Austria
e-mail: josef.fuessl@tuwien.ac.at

- *RVE approach:* the effective media theory, on the other hand, is based on the introduction of a representative volume element (RVE), stipulating the separation of observation scales. The size of an RVE must be (i) considerably larger than the characteristic dimension of the material phases forming the material at the considered scale and (ii) significantly smaller than the material or material phase built up by the RVE.

For most materials exhibiting a matrix-inclusion morphology, which are in general obtained by mixing, pouring and, if necessary, compaction/densification, the irregular arrangement of the microstructure renders the RVE approach as appropriate. Hereby, the response of the considered RVE may be computed numerically or analytically. As regards the latter, averaging schemes, such as, e.g., schemes developed within the framework of continuum micromechanics, may be employed for upscaling of elastic and viscoelastic properties (see, e.g., [1], [2]). Recently, the range of application of averaging schemes was extended towards upscaling of strength properties, representing the elasto-plastic behavior of the material by a secant-elastic law [3]–[5]. Hereby, failure of the entire RVE is assumed. In general, however, material failure is characterized by the development of a localized failure zone, introducing a new length scale in the RVE (see Fig. 1). Moreover, localized failure results in the violation of the continuous boundary field enforced in averaging schemes. Compared to analytical methods, the finite element method (FEM) is able to take localized material failure into account. However, in case of upscaling by means of the FEM, the complete load history must be considered. Moreover, in order to predict the correct failure mechanism, softening and, thus, suitable regularization techniques must be incorporated into the FEM approach.

The discretized version of limit analysis, on the other hand, concentrates on the instant of material failure. First publications on limit analysis dealing with efficient non-linear solution algorithm date back to 1993 [6].

In the following section, the discrete formulation of limit analysis for determination of lower and upper bounds for failure loads will be briefly assessed, following [7] and [8] as well as the formulation of the underlying optimization problem as a second-order-cone-programming (SOCP) problem. The performance of the proposed upscaling approach for the case of uniaxial loading states will be investigated in Sect. 3. The appropriate choice for the RVE for the case of material failure in matrix-inclusion morphologies will be discussed. Finally, the influence of the material morphology and of degradation processes in matrix-inclusion materials on strength properties (uniaxial tensile and compressive strength) as well as on effective failure criteria will be investigated, providing new insight into the microstructure-triggered failure mechanisms of composite materials.

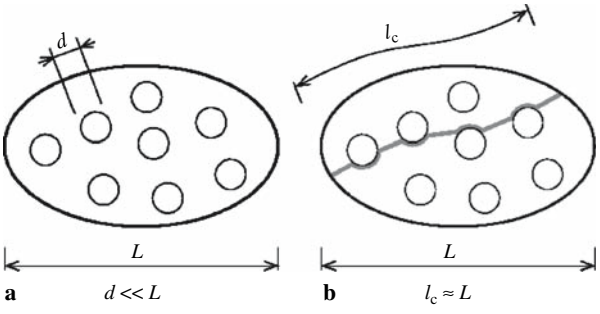

Fig. 1. Separation of scales within the RVE approach: **a** appropriate and **b** inappropriate configuration for upscaling by means of averaging schemes

2 Discretized form of limit analysis

Originally, the objective of limit analysis was determination of the load-bearing capacity of structures exhibiting elastoplastic material response. At collapse, the capacity of structures to store additional external work as recoverable energy is exhausted. For a given macroscopic strain-rate field and a prescribed macroscopic stress field defining the loading situation, limit analysis concentrates on the critical work rate at failure of structures or, as in the present case, of composite materials. The problem may be stated as follows: find the admissible velocity field, which minimizes the internal dissipated energy over the set of all statically admissible stress fields, which maximize the internal dissipated energy. Unfortunately, the so-obtained saddle-point problem can be solved only for simple geometric and loading situations, and simple material behavior. For the case of more complex situations, the plastic-flow compatibility in the so-called static principle, on the one hand, or the static equilibrium and the plastic admissiblity in the so-called kinematic principle, on the other hand, may be relaxed, providing access to lower and upper bounds for the applied macroscopic stress field.

2.1 The kinematic approach – the upper-bound formulation

For the numerical upper-bound (UB) formulation, triangular elements with linear shape functions for the interpolation of the unknown velocity field are used. In order to consider velocity discontinuities, unlike as in standard discretization methods such as the FEM, each node is assigned to one element only [9]. For the stress field, on the other hand, a constant stress distribution is assumed within each element. To enforce the admissibility of the velocity field solution within the UB formulation, the following conditions are imposed:

- Within each element, the strain rate must follow an associative flow rule

$$\dot{\boldsymbol{\varepsilon}} = \dot{\lambda}\frac{\partial f}{\partial \boldsymbol{\sigma}}, \tag{1}$$

  where $\dot{\boldsymbol{\varepsilon}}$ represents the strain-rate tensor, and $\dot{\lambda}$ is the plastic multiplier, satisfying $\dot{\lambda} \geq 0$.
- Normal and tangential velocity jumps, $[u_n]$ and $[u_t]$, across each discontinuity must satisfy the flow rule

$$[\![u_n]\!] = |[\![u_t]\!]| \tan\varphi, \tag{2}$$

  where φ denotes the angle of internal friction.
- The velocity must satisfy the boundary conditions $\mathbf{u} = \bar{\mathbf{u}}$ on the boundary A_u, on which velocities are prescribed.
- Moreover, the rate of flow of material through the boundary A is set to a prescribed value.

  Under these conditions, the internal rate of work

$$\dot{W}^{int} = \sum_{e=1}^{n_e}\left(\dot{\lambda}\frac{\partial f}{\partial \boldsymbol{\sigma}^T}\boldsymbol{\sigma}\right)^e + \sum_{i=1}^{n_i}\left(\mathbf{c}^T\dot{\boldsymbol{\gamma}}\right)^i \tag{3}$$

  is minimized. In Eq. (3), the first part considers the contribution to $\dot{W}^{int}$ within the elements and $(\mathbf{c}^T\dot{\boldsymbol{\gamma}})^i = \int_{l_i} c_i[\mathbf{u}]^i dl$ is the contribution of the ith discontinuity with $[\mathbf{u}]^i$ as the velocity jump in the discontinuity i. Hereby, c_i is the cohesion and $\dot{\boldsymbol{\gamma}}$ the plastic multiplier associated with the ith discontinuity.

2.2 The static approach – lower-bound formulation

For the numerical lower-bound (LB) formulation, the finite elements used in the UB formulation are employed. However, in the LB formulation, the nodal unknowns are the stress tensors, allowing jumps of the tangential stress component along element edges [10]. To enforce equilibrium and to render the stress-field solution admissible, the following conditions are imposed:

- Within each element, equilibrium is enforced by $\mathrm{div}[\boldsymbol{\sigma}(\mathbf{x})] = \mathbf{g}$, where $\mathbf{g}$ are prescribed body forces.
- At discontinuites, continuity of normal- and shear-stress components is enforced.
- The stress field must satisfy the boundary conditions $\boldsymbol{\sigma}(\mathbf{x}) \cdot \mathbf{n}(\mathbf{x}) = \alpha\bar{\mathbf{t}}$ on the boundary A_t, on which surface tractions $\bar{\mathbf{t}}$ are prescribed. $\mathbf{n}(\mathbf{x})$ denotes the outward normal unity vector on A_t.
- Moreover, the stress field associated with plastic collapse has to satisfy $f(\mathbf{x}; \boldsymbol{\sigma}(\mathbf{x})) \leq 0$, where f denotes the yield function. Because of the linear interpolation of the nodal stresses $\mathbf{q}_\sigma$, the yield function is satisfied everywhere in the element if it is satisfied at its nodes.

Under these conditions, the external rate of work $\dot{W}^{ext} = \alpha$ is maximized.

Considering a dual form of the UB optimization problem [7], formulated in terms of stresses, a form of the UB and LB optimization problem may be obtained, that is mathematically similar, and reads

$$\max\{\alpha\}, \tag{4}$$

with linear constraints of the form

$$\mathbf{A}_1\mathbf{x}_1 = \mathbf{b}_1 \quad \text{and} \quad \mathbf{A}_2\mathbf{x}_2 \leq \mathbf{b}_2, \tag{5}$$

enforcing the aforementioned conditions for kinematic admissibility and static equilibrium in the UB and LB formulation, respectively. In both the stress-based UB and LB optimization problem, the stress state is constrained by the yield function, i.e.,

$$f(\mathbf{q}_\sigma) \leq \mathbf{0}. \tag{6}$$

Because of the similarity of the UB and LB formulation, the same solution algorithm can be applied.

2.3 Failure criteria and solution of optimization problem

The optimization problem (4) to (6) is non-linear, with the non-linearity introduced by the yield functions $f(\mathbf{q}_\sigma)$. Thus, if all yield functions are convex, the optimization problem itself will be convex. In this case, only one optimum exists. It is the global optimum. In recent years, different non-linear-convex optimization strategies were applied to limit-analysis problems: in [10], a two-stage-quasi-Newton algorithm is employed. It consists of linearizing the optimality conditions and solving the resulting linear system iteratively. In [11], another interior point method, based on the logarithmic barrier function, is used. Furthermore, a sequential-quadratic-programming scheme may be used to solve the underlying quadratic optimization problem by the primal-dual interior point solver described in [12]. In case of yield surfaces exhibiting corners and edges, and thus becoming non-differentiable, smoothing of the yield surface was proposed in [13]. In case of cone-shaped yield criteria (such as, e.g., the Mohr–Coulomb criterion in plane strain and the Drucker–Prager criterion in 2D and 3D condition), SOCP was used in [8], [14] and [15]. Hereby,

the conic optimization problem[1] is solved efficiently by an interior point method. In this paper, the SOCP algorithm outlined in [17], which was implemented into the optimizer MOSEK [18], is used. Hereby, yield criteria having the form

$$f = \sqrt{\mathbf{q}_\sigma^T \mathbf{M} \mathbf{q}_\sigma} + \mathbf{m}^T \mathbf{q}_\sigma - k \leq 0, \tag{11}$$

or, equivalently,

$$\sqrt{\mathbf{q}_\sigma^T \mathbf{M} \mathbf{q}_\sigma} \leq k - \mathbf{m}^T \mathbf{q}_\sigma, \tag{12}$$

where $\mathbf{M}$ is at least positive semi-definite, are used for constraining stress states. The cone formulation of Eq. (12) is obtained by introducing [16]

$$\mathbf{M} = \mathbf{L}^T \mathbf{L}, \quad \mathbf{y} = \mathbf{L}\mathbf{q}_\sigma, \quad \text{and} \quad z = k - \mathbf{m}^T \mathbf{q}_\sigma, \tag{13}$$

giving

$$\sqrt{\mathbf{y}^T \mathbf{y}} \leq z, \tag{14}$$

where $\mathbf{L} \in R^{h \times d}$ ($h = \text{rank}(\mathbf{M})$, $d =$ dimension of $\mathbf{q}_\sigma$) and $\mathbf{y}$ and z are auxiliary variables. The cone formulation (13) and (14) for the employed Mohr–Coulomb criterion for plane strain and plane stress is given in the Appendix.

3 Effect of arrangement and size of inclusions on uniaxial tensile strength and failure mode

In this section, limit analysis is applied to composite material systems subjected to uniaxial tensile loading. Hereby, different matrix-inclusion morphologies are discretized (see, e.g., Fig. 2) and different strength properties are assigned to the matrix, the inclusion, and the interfaces. By means of limit analysis, bounds for the uniaxial tensile strength are computed. All material systems are discretized with approximately 5,000 2D elements. The matrix and the particles (if present) obey the Tresca failure criterion with a cohesion ratio c_p/c_m of the particles and the matrix equal to 10. In

[1] A general conic optimization problem consists of a linear objective function

$$\min\{\mathbf{c}^T \mathbf{x}\}, \quad \text{with} \quad \mathbf{x} \in \mathbf{R}^n, \tag{7}$$

subjected to (i) a set of linear constraints $\mathbf{A}\mathbf{x} = \mathbf{b}$ and (ii) the conic constraints $\mathbf{x} \in \mathcal{C}$, where $\mathcal{C}$ is a closed convex pointed cone. A set $\mathcal{C}$ is called a cone if $\forall \mathbf{x} \in \mathcal{C}$ and $\lambda \geq 0$, $\lambda \mathbf{x} \in \mathcal{C}$. Examples of such cones are

- the non-negative orthant

$$\mathcal{C} = \mathcal{R}_+ = \{x : x \geq 0\}, \tag{8}$$

- the second-order (or ice-cream) cone

$$\mathcal{C} = \left\{ \mathbf{x} \in \mathcal{R}^m : \sqrt{\sum_{i=2}^{m} x_i^2} \leq x_1, \quad x_1 \geq 0 \right\}, \tag{9}$$

- and the rotated quadratic cone

$$\mathcal{C} = \left\{ \mathbf{x} \in \mathcal{R}^m : \sum_{i=3}^{m} x_i^2 \leq 2x_1 x_2, \quad x_1 \geq 0, \quad x_2 \geq 0 \right\}. \tag{10}$$

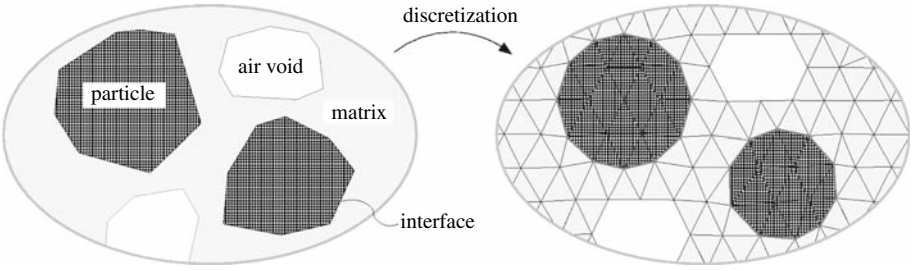

Fig. 2. Illustration of the discretization of a heterogeneous material for the application of limit analysis

order to investigate the effect of the arrangement of inclusions on the tensile strength, the angle β between the line connecting two inclusions (in a first step, only two inclusions are considered in this study) and the direction of loading was varied. Three different types of material systems were investigated:

1. *Effect of arrangement of air voids:* Fig. 3a shows the influence of β on the upper and lower bound of the tensile strength of a material with two air voids (see Fig. 3b). For all three air-void contents f_a considered in this study, the largest values for the tensile strength are obtained for

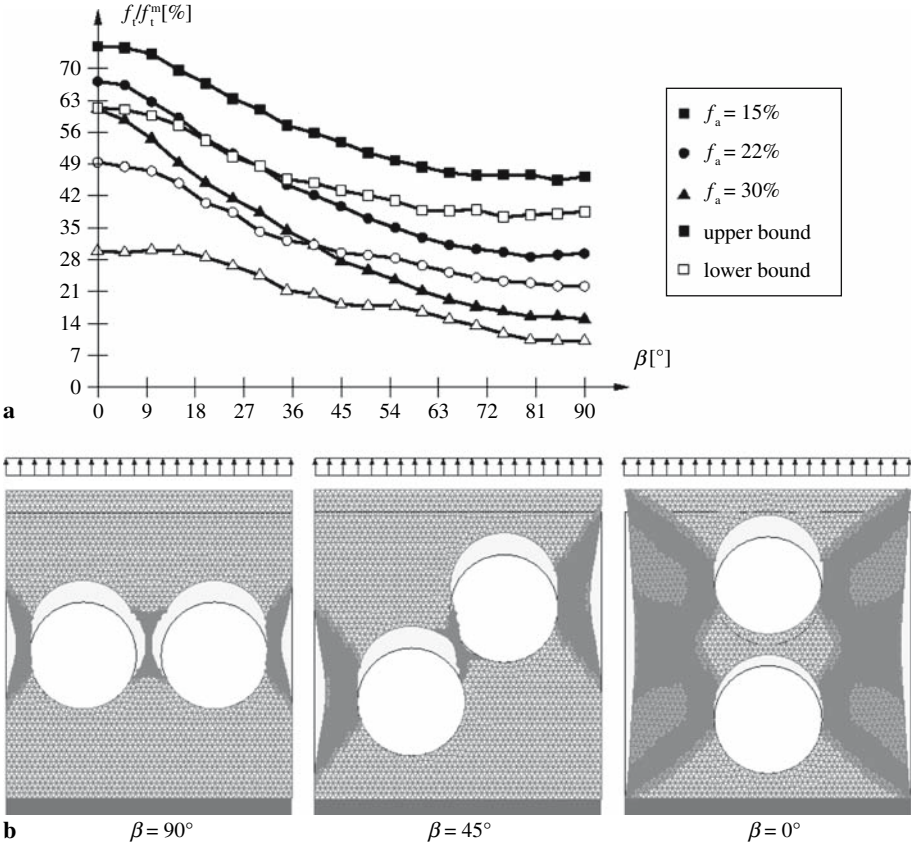

Fig. 3. a Influence of β on the upper and lower bound of the tensile strength of a material with two air voids; **b** plastic failure zones obtained from upper-bound calculations for $f_a = 22\%$ (f_a, air-void content; f_t, tensile strength of composite material; f_t^m, tensile strength of matrix material)

$\beta = 0°$ and the smallest ones for $\beta = 90°$. The difference between the tensile strength obtained from the LB and UB formulation, referred to as "bound gap", increases with increasing air-void content f_a. The influence of the air-void arrangement on the estimated tensile strength of the porous material is up to 50%.

2. *Effect of arrangement of particles:* for the same matrix material reinforced with two particles, the tensile strength obtained from the UB formulation is illustrated in Fig. 4a. In contrast to the situation with air voids, the smallest value for the tensile strength is obtained for $25° < \beta < 45°$. This range of β corresponds with the orientation of slip lines for tensile failure modeled by the Tresca criterion ($45°$). An arrangement of particles in this range provides a proper path for the failure mode through the reinforcing particles, explaining the small values for the tensile strength. Again, a great influence of the arrangement of the inclusions on the tensile strength is observed. Three failure modes, explaining this influence, are shown in Fig. 4b.
3. *Effect of arrangement of particles with degraded interfaces:* for the case of degraded interfaces between the matrix and the particles, the influence of β on the tensile strength is illustrated in Fig. 5a. Failure of interfaces is modeled by the Mohr–Coulomb criterion with a cohesion of $c_I = c_m/10$ and a friction angle of $20°$. Based on the obtained results, weakening of the interfaces compensates the reinforcing effect of particles. Thus, the dependence of the tensile strength on β is similar to the situation of a material containing air voids (see Fig. 3). Even the failure mechanisms for air voids and particles with degraded interfaces are similar (compare Figs. 3b, 5b). The presented results show a considerable influence of the choice of the RVE, defined by arrangement of the inclusions, on the tensile strength of the composite. This was the

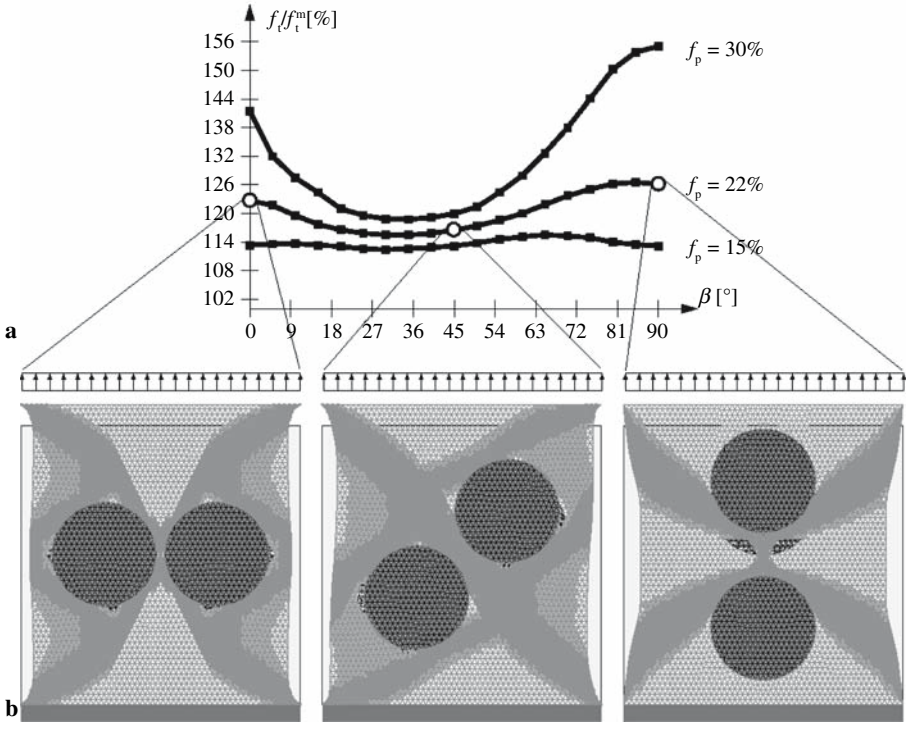

Fig. 4. **a** Influence of β on the upper bound for the tensile strength for a material with two particles, **b** plastic failure zones from upper-bound calculations (f_p, particle content; f_t, tensile strength; f_t^m, tensile strength of matrix material)

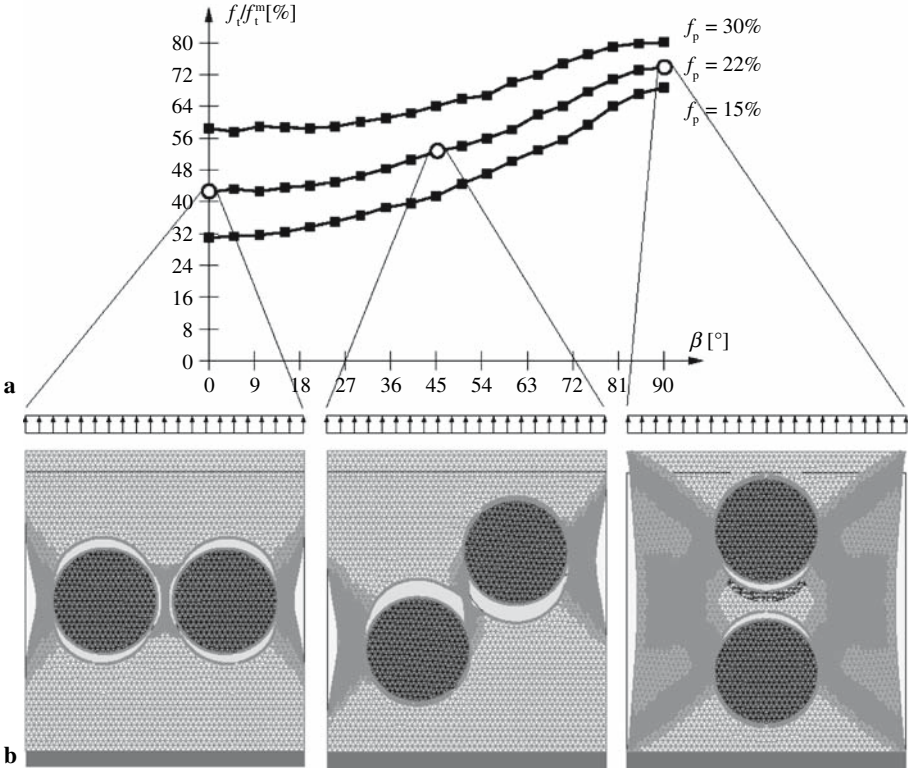

Fig. 5. a Influence of β on the upper bound of the tensile strength of a material with two particles characterized by degraded interfaces; **b** plastic failure zones obtained from upper-bound calculations (f_p, particle content; f_t, tensile strength of the composite; f_t^m, tensile strength of matrix material)

motivation for the investigation of more complex material microstructures, focusing on the influence of the arrangement of air voids and inclusions and the size of the RVE on the effective strength. In the following study, only material microstructures with a volume fraction of $f_a = 25\%$ and $f_p = 25\%$, respectively, are considered. However, they are represented by different numbers of inclusions, ranging from 2 to 50. For each number of inclusions, ten different arrangements are considered and the corresponding upper and lower bounds for the tensile strengths are computed.

- Figure 6 shows the result for a material with air voids with an air-void content of $f_a = 25\%$. Independent of the number of air voids, the average effective strength is nearly constant. However, the scatter resulting from different arrangements of air voids considered in this study becomes smaller with increasing number of voids and, thus, with increasing RVE-size/void-size ratio. In contrast to upscaling of elastic properties, because of the highly localized failure modes which depend on the arrangement of air voids, upscaling of strength seems to depend less on the RVE-size/void-size ratio, whereas the particle arrangement results in a significant scatter.
- The same study was conducted for a material reinforced with particles (see Fig. 7). The observed scatter of the upper bound for the tensile strength decreases with increasing number of inclusions, with a maximal scatter of 6% if the number of particles is greater than 35. Additionally, the average tensile strength slightly increases, which is explained by the increased probability of particles obstructing the development of the failure mechanism. The

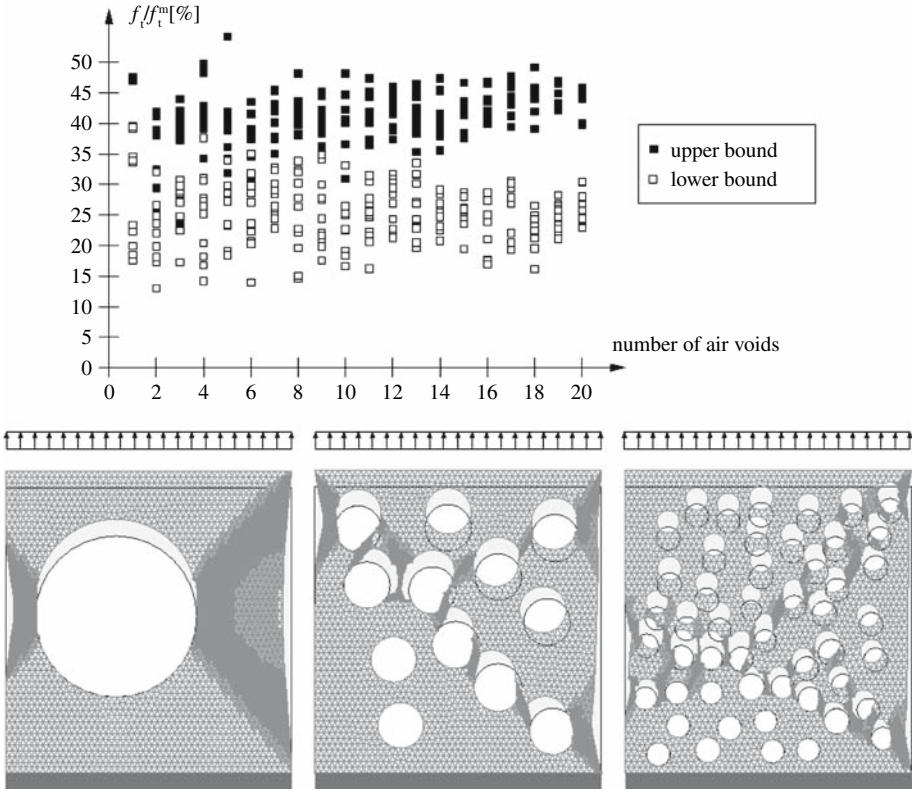

Fig. 6. Influence of RVE size on the effective tensile strength of a material with air voids ($f_a = 25\%$, air-void content; f_t, tensile strength of the composite; f_t^m, tensile strength of matrix material)

lower bounds are close to the tensile strength of the matrix, with the failure mode developing close to the loading platen. As a remedy, additional particles may be placed at the loaded boundary of the RVE. The RVE considered in the lower-bound formulation is not able to capture the strengthening effect of the particles appropriately.

- In the previous study, the same strength properties were assigned to the matrix material and the interface between the matrix and the particles. Introducing degraded interfaces, with $c_I = c_m/10$ and $\varphi_I = 20°$, leads to the results shown in Fig. 8. Compared to the results in Fig. 7, a considerable decrease of the macroscopic strength is obtained. The scatter of results and the increase of the tensile strength with increasing number of particles is similar to the situation in the previous study.

4 Application to selected material microstructures

In summary, the scatter of the estimated tensile strength of the composite material in consequence of the arrangement of the inclusions was greater than the influence of the RVE-size/inclusion-size ratio. In fact, marginal changes of the tensile strength for an RVE-size/inclusion-size ratio greater than five were observed. Accordingly, for the studies reported in this section, which are characterized by inclusions of varying size, the size of the RVE was adopted according to the result from the previous study.

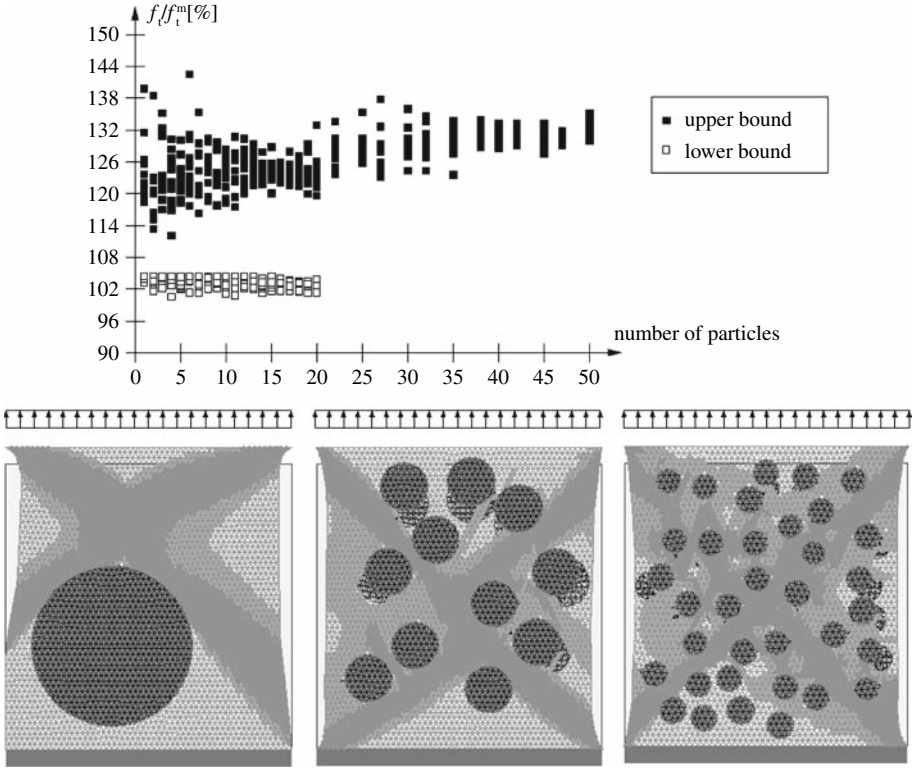

Fig. 7. Influence of the RVE size on the effective tensile strength of a material with particles ($f_p = 25\%$, particle content; f_t, tensile strength of the composite; f_t^m, tensile strength of matrix material)

4.1 Uniaxial loading situation

Figure 9a illustrates the decrease of the tensile strength as a function of the volume fraction f_a of the air voids. Failure of the matrix material is described by the Tresca criterion. The so-called bound gap, defined as the difference between the upper- and the lower-bound of the collapse load, is about 19%, and, therefore, compared to the scatter observed in the experimental results, of acceptable magnitude. The largest influence of the air void configuration (about 15%) is obtained for a volume fraction between 10 and 20%. Figure 9b shows the plastic zones corresponding to the lower-bound, and Fig. 9c the plastic zones and the failure mechanism obtained from the upper-bound formulation. The principal collapse mechanism develops along the most weakened path through the material system by connecting air voids in order to form the failure zones. For an air-void content of 20%, the decrease of the tensile strength is already 50% compared to the tensile strength of the matrix. Figure 10a illustrates the influence of the volume fraction of particles and the effect of the displacement boundary condition (horizontal displacement at the top boundary) on the upper bound of the tensile strength. For the description of failure of both material phases, the Tresca criterion is employed, with a cohesion ratio of $c_p/c_m = 10$. If the horizontal movement of the loaded boundary is restrained (see Fig. 10c), the flexibility of the material microstructure is reduced and, thus, the failure mechanism is located at the middle of the RVE. This results in an increase of the collapse load of about 5%. Figure 11a contains upper bounds of the tensile strength as a function of the cohesion ratio c_p/c_m, ranging from one to three, and for three different particle contents. The obtained results show that up to a strength ratio of 2.8, the failure mode is associated with failure of both matrix and particles (see Fig. 11b, c). For a strength ratio c_p/c_m greater than 2.8 (see Fig. 11a),

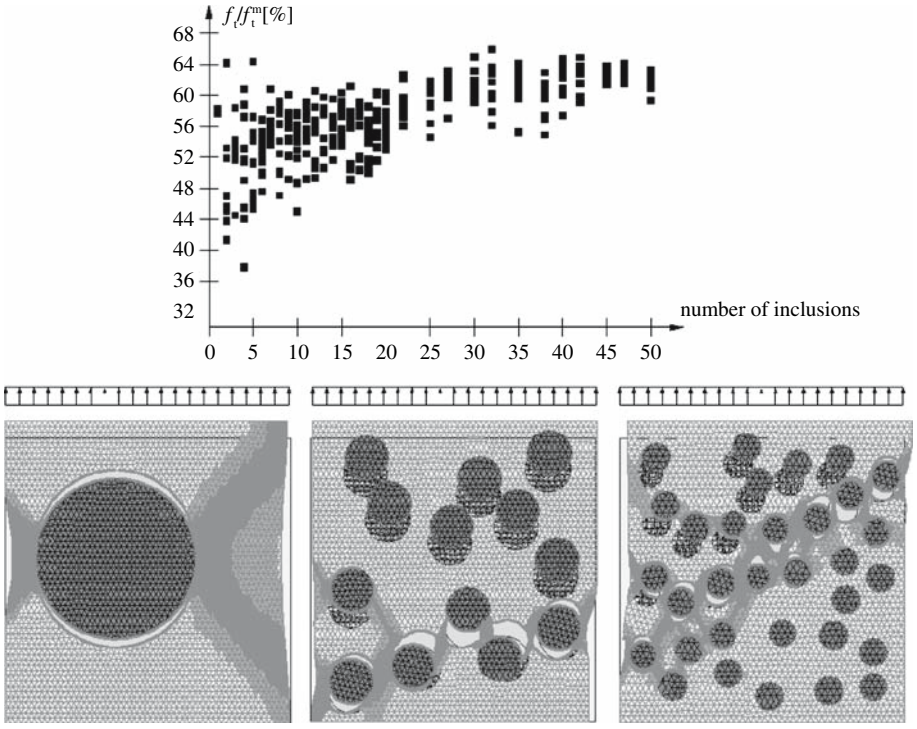

Fig. 8. Influence of the RVE size on the effective tensile strength of a material with particles, characterized by degraded interfaces ($f_p = 25\%$, particle content; f_t, tensile strength of the composite; f_t^m, tensile strength of matrix material)

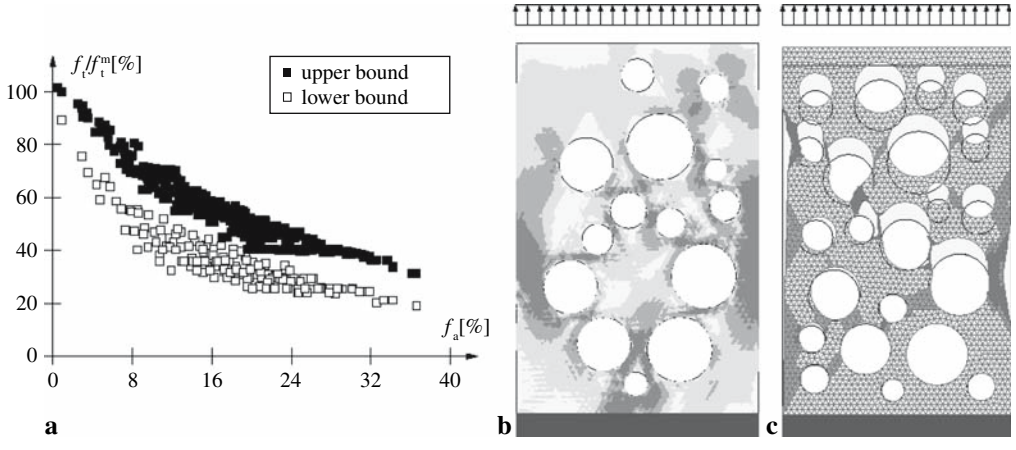

Fig. 9. **a** Tensile strength as a function of the air-void content f_a for circular air voids characterized by varying size; **b** plastic zones (LB) $f_a = 25\%$; **c** failure mechanism (UB) $f_a = 37\%$

failure occurs exclusively in the matrix phase. Thus, no further increase of the tensile strength is observed for an increasing particle strength c_p. Figure 12 illustrates upper bounds of the compressive strength as a function of the friction angle φ_I of the interfaces. Similar to a previous study, two different boundary conditions are investigated. Again, restraining the horizontal displacement at the

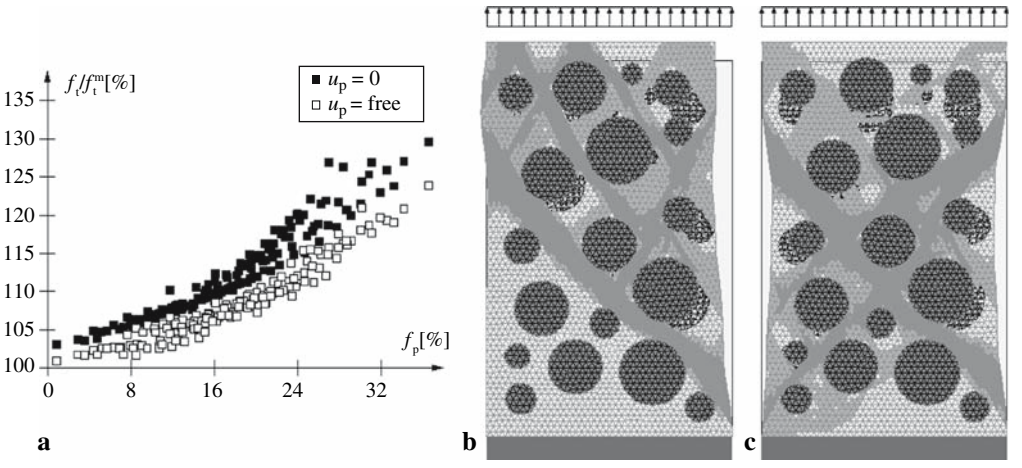

Fig. 10. **a** Tensile strength as a function of the volume fraction of rigid particles, f_p, and boundary condition u_p at the loaded boundary; failure mechanism (UB) for $f_p = 37\%$: **b** $u_p =$ free and **c** $u_p = 0$

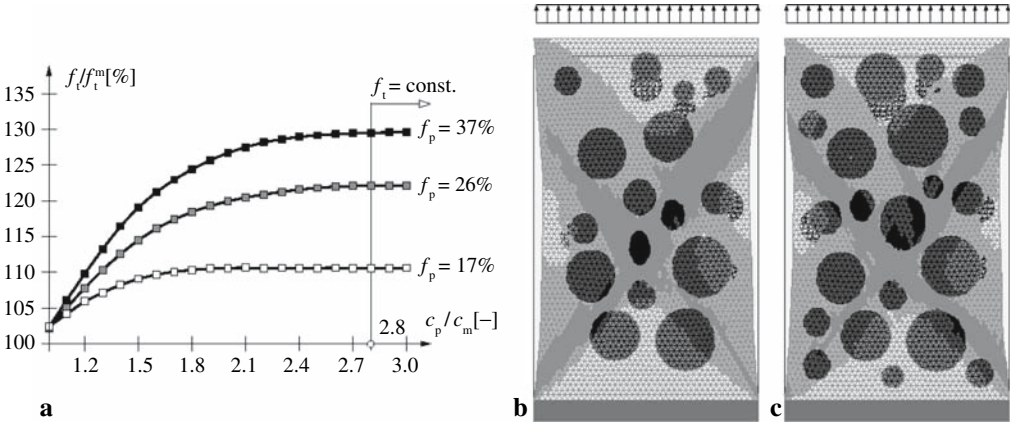

Fig. 11. **a** Tensile strength as a function of the particle/matrix-strength ratio; failure mechanism (UB): **b** $f_p = 26\%$, $c_p/c_m = 1.5$ and **c** $f_p = 37\%$, $c_p/c_m = 1.5$

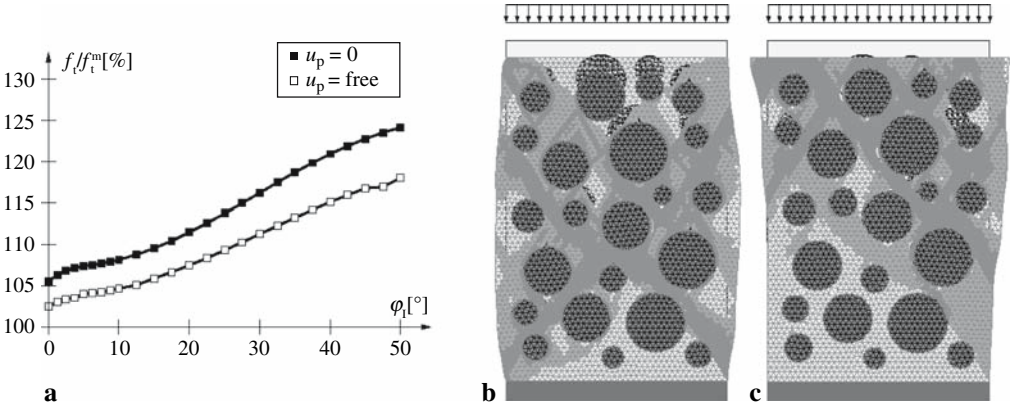

Fig. 12. **a** Compressive strength as a function of the friction angle φ_I at the matrix/particle-interface and boundary condition u_p at the loaded boundary; failure mechanism (UB) for $f_p = 37\%$: **b** $u_p = 0$, $\varphi_I = 30°$ and **c** $u_p =$ free, $\varphi_I = 50°$

top boundary leads to a higher strength of the composite material (approximately 5%). Temperature changes in matrix/particle-composites, characterized by different thermal-dilation behavior for the matrix and the particles, may result in eigenstresses leading to debonding effects at the particle/matrix-interface. Figure 13b and c show upper-bound results for matrix/particle-composites with material interfaces weakened by a reduction of the cohesion, with $c_p/c_I = 10$, considering increased values for the friction angle at the interfaces. Figure 13a shows the decrease of the tensile strength as a function of the friction angle of the interfaces. With increasing volume fraction of the particles, resulting in a greater number of interfaces to be incorporated into the failure mechanism, the tensile strength of the composite material decreases. The possibility of reducing the strength properties of the interfaces allows consideration of debonding between particles and the matrix during upscaling. Figure 14a shows upper-bound results for the tensile strength for different crack densities, defined by the dimensionless parameter $d = \sum_{\mathrm{N_{cracks}}}(\text{crack length})^2/\text{area}$. Hereby, the failure mechanism is composed by plastic failure zones developing between the existing microcracks, with the latter strongly affecting the failure mechanism. For example, both a diffuse failure (Fig. 14b) and a distinct

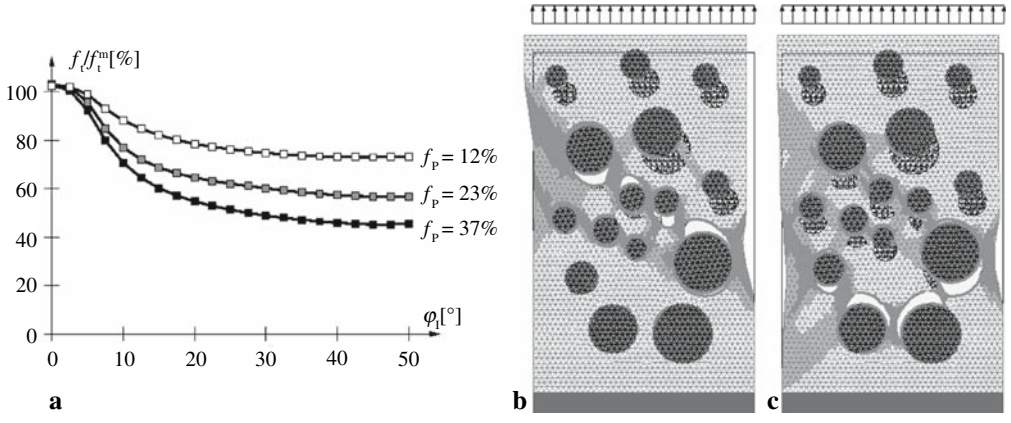

Fig. 13. **a** Tensile strength as a function of the friction angle of the matrix/particle-interface in case of degraded interfaces; failure mechanism (UB) for $f_p = 23\%$: **b** $\varphi_I = 20°$ and **c** $\varphi_I = 30°$

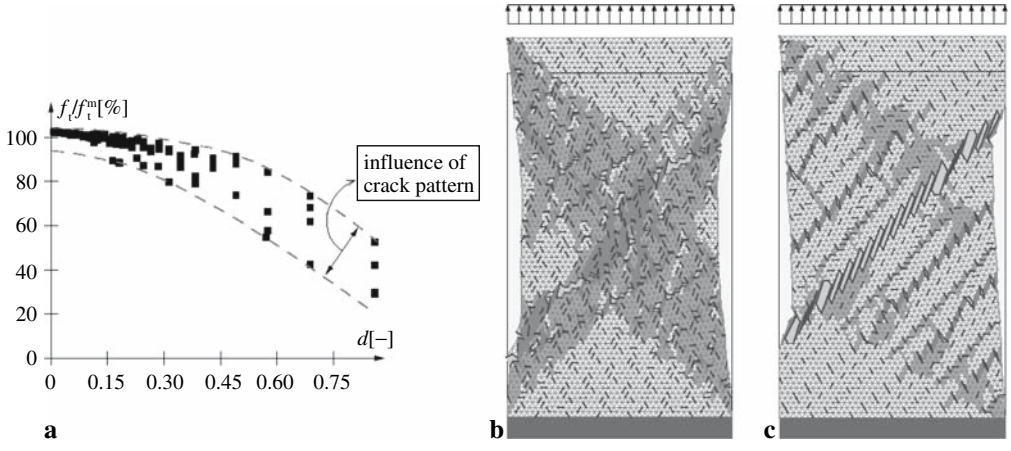

Fig. 14. **a** Tensile strength as a function of the crack density; **b** diffuse failure mechanism (UB); **c** development of failure surface (UB)

failure surface (Fig. 14c) were obtained for the same crack density. For great crack densities, the influence of the crack pattern leads to a scatter of the tensile strength of about 25%.

4.2 Two-dimensional loading situation

In this subsection, the proposed upscaling scheme is applied to biaxial-loading situations. In order to enable the formation of proper failure modes, tangential velocity jumps are allowed at each point of the boundary of the RVE. Thus, the condition $\mathbf{E} = \langle \boldsymbol{\varepsilon} \rangle_V$ ($\mathbf{E}$ is the macroscopic strain and $\langle \boldsymbol{\varepsilon} \rangle_V$ denotes the average of the microscopic strains over the body V), which is essential if averaging techniques are used, is not enforced anymore. The obtained results are plotted in the principle-stress (Σ_1/Σ_2)-plane, giving upper and lower bounds for the effective failure surface:

- In Fig. 15, an upper and a lower bound of the effective failure surface of a porous material, with an air-void content of $f_a = 27\%$, is given. Hereby, the Tresca criterion for plane strain, with a uniaxial strength equal to $2c$, is assigned to the matrix. The presence of air voids allows for dilation and compaction of the RVE, giving a yield surface bounding the space of admissible stress states for every biaxial loading situation. On the contrary, the Tresca criterion (plane strain) for a homogeneous material (dashed line) is unbounded for $\Sigma_1 = \Sigma_2$, resulting from the restriction to in-plane failure modes in case of plane strain.
- Figure 16 shows an upper and a lower bound of the effective failure surface for the plane-stress case of the same material system as before. In contrast to the plane-strain situation, the material system becomes more flexible, yielding a larger reduction of the effective strength of the porous composite. The aforementioned greater flexibility of the material system is evident for the failure modes for $\Sigma_1 \approx \Sigma_2$. In contrast to the failure mode obtained for the plane-strain study (Fig. 15), the width of the failure mode is significantly smaller in the plane-stress situation (Fig. 16).

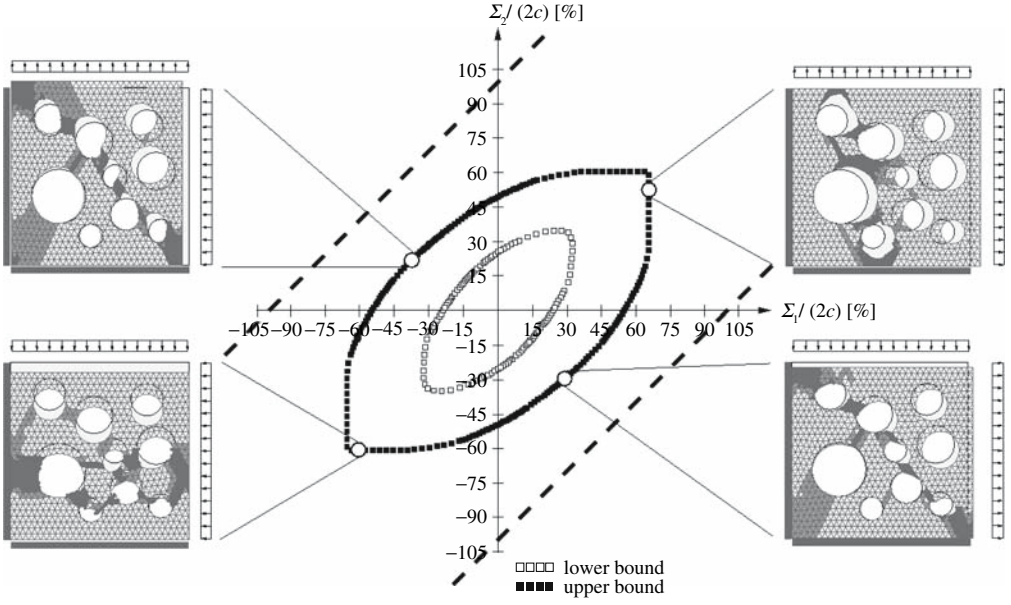

Fig. 15. Lower and upper bound for effective failure surface of a porous material (plane-strain situation) with different biaxial failure modes (UB)

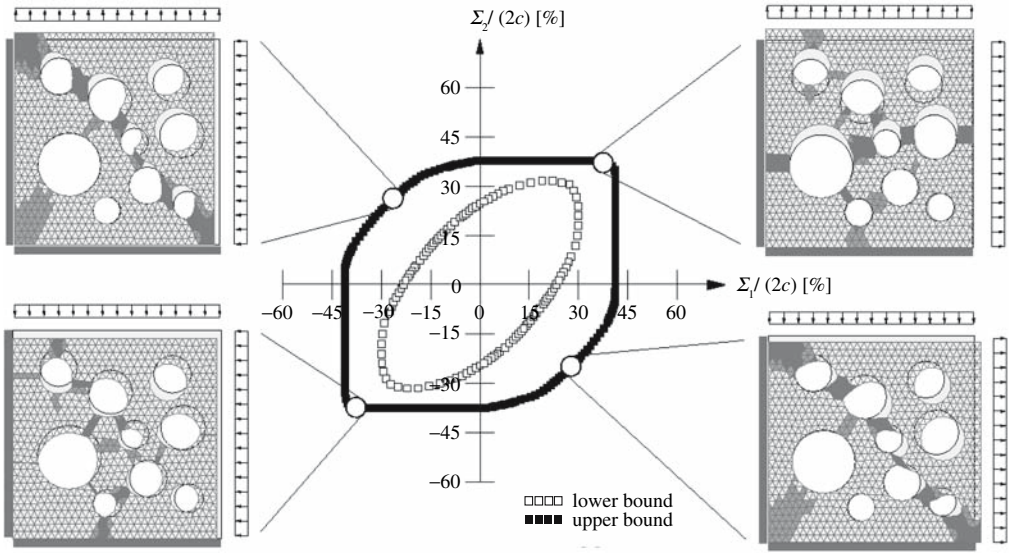

Fig. 16. Lower and upper bound for effective failure surface of a porous material (plane-stress situation) with different biaxial failure modes (UB)

- As mentioned in the previous subsection, failure of matrix–particle materials is often influenced by degraded interfaces between the matrix and the particles. In Fig. 17, upper bounds of effective failure surfaces for (a) the plane-strain and (b) the plane-stress situation are given for a weakened matrix–particle material. Hereby, failure at the interface is described by the Mohr–Coulomb criterion, with $c_m/c_I = 10$ and $\varphi_I = 20°$. Both the matrix and the particles obey the Tresca criterion with $c_p/c_m = 10$. The grey-shaded areas in the principal-stress planes show the decrease of strength as a consequence of interface degradation.

5 Conclusions and outlook

In contrast to upscaling of elastic properties of composites characterized by a randomly-distributed microstructure, where a smooth displacement field is assumed within the representative volume element (RVE), upscaling of material failure is associated with a highly localized collapse mechanism affecting both the bulk and the boundary deformations of the RVE. Accordingly, standard mean-field techniques used in homogenization of elastic and viscoelastic properties cannot be transferred to homogenization of strength properties.

In this paper, numerical limit-analysis was proposed for upscaling of material failure, suitable for capturing complex mechanisms as observed in matrix-inclusion materials. The performance of the proposed upscaling technique was illustrated by different investigations, focusing on the effect of air voids and particles, degradation of interface properties, and of microcracks on the material strength. Based on the obtained results, the following conclusions can be drawn:

- As regards the size of the RVE employed in limit analysis, the RVE-size/inclusion-size ratio appeared to have only little influence on the strength of the composite material.
- On the other hand, the arrangement of the inclusions has a significant influence on the material strength. This was reflected by the large scatter of the numerical results obtained for the tensile strength of the composite material. However, this scatter decreased with increasing RVE-size/inclusion-size ratio.

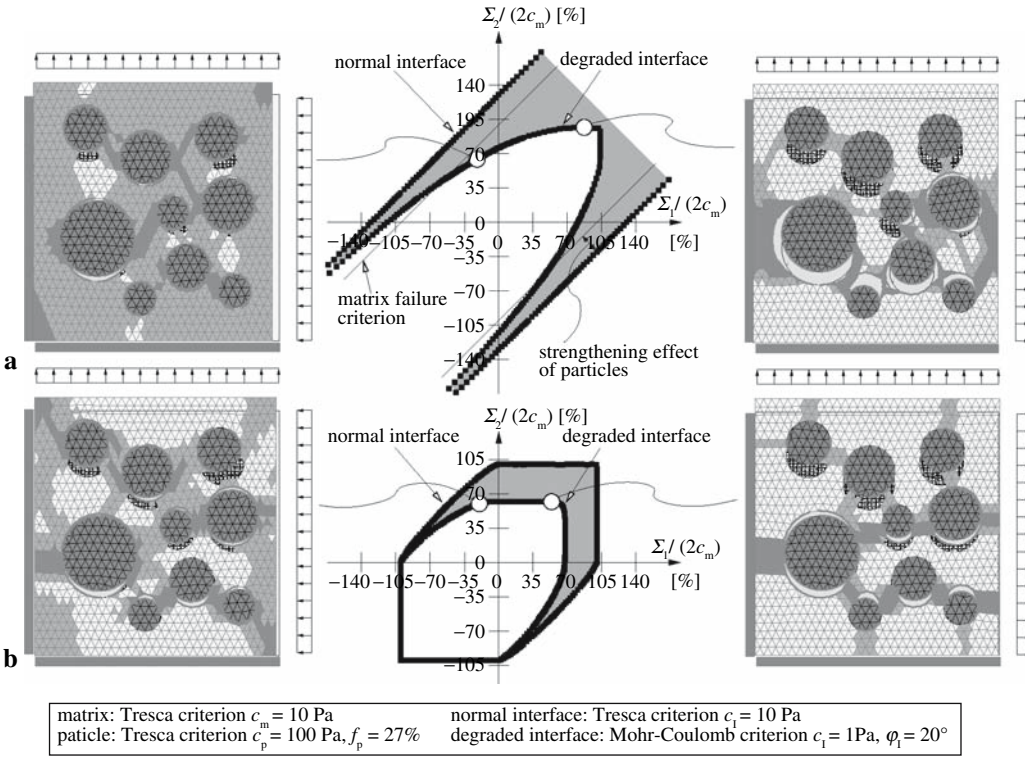

Fig. 17. Influence of interface degradation on effective failure surface for **a** plane-strain situation and **b** plane-stress situation

- In case of intact interfaces between particles and the matrix, the presence of particles leads to an improvement of strength properties of the composite material. Interestingly, this improvement, which is greater for increasing strength properties of the particles, remains constant for a particle strength 2.8-times greater than the strength of the matrix material. In fact, for strength ratios greater than 2.8, failure occurs exclusively in the matrix phase.
- The degradation of strength properties at the interface between the particles and the matrix, which is often observed in matrix–particle materials, resulted in a significant decrease of the strength of the composite material. The aforementioned improvement of strength properties in consequence of the presence of particles was compensated by the degradation process, with the particles acting as air voids rather than as reinforcement. This fact led to similar failure modes as observed for the material with air voids.
- The strength of a material damaged by microcracks was found to be influenced by both the number and length of cracks, giving the crack density d, and the arrangement of the microcracks. As a function of the latter, either diffuse failure or the development of localized failure surfaces was observed.

Finally, the developed upscaling scheme was employed for determination of microstructure failure surfaces, considering plane-stress and plane-strain situations. In this context, current research work is devoted to the extension of the presented upscaling scheme to 3D microstructures, considering up to 30,000 higher-order elements [19]. Moreover, an extension of the 2D approach, considering up to 60,000 elements, will lead to bound gaps of approximately 3–5%. This extensions allow to assess the quality of different upscaling schemes based, e.g., on averaging techniques.

Appendix

Second-order-cone formulation of the Mohr–Coulomb criterion

- *Mohr–Coulomb criterion (plane strain):* the Mohr–Coulomb failure criterion for the plane-strain situation reads

$$f_{MC} = \sqrt{(\sigma_{xx} - \sigma_{yy})^2 + 4\sigma_{xy}^2} + (\sigma_{xx} + \sigma_{yy}) \sin\varphi - 2c\cos\varphi \leq 0, \tag{A.1}$$

  where c denotes the cohesion and φ the friction angle. Considering

$$\sigma_m = \frac{1}{2}(\sigma_{xx} + \sigma_{yy}) \quad \text{and} \quad s_{ij} = \sigma_{ij} - \sigma_m \delta_{ij}, \tag{A.2}$$

  where δ_{ij} is Kronecker's δ, the yield criterion (A.1) may be rewritten as

$$f_{MC} = \sqrt{s_{xx}^2 + s_{xy}^2} + \sigma_m \sin\varphi - c\cos\varphi \leq 0. \tag{A.3}$$

  Based on the yield criterion (A.3), the quantities of the respective cone formulation read

$$\mathbf{L} = \begin{bmatrix} 1 & 0 \\ 0 & 1 \end{bmatrix}, \quad \mathbf{y} = \begin{Bmatrix} y_1 \\ y_2 \end{Bmatrix}, \quad \mathbf{q}_\sigma = \begin{Bmatrix} s_{xx} \\ s_{xy} \end{Bmatrix} \quad \text{and} \quad z = c\cos\varphi - \sigma_m \sin\varphi. \tag{A.4}$$

- *Mohr–Coulomb criterion (plane stress):* for the plane-stress situation, in addition to (A.3) the stress state is constrained by

$$\sqrt{s_{xx}^2 + s_{xy}^2} + \sigma_m - \frac{2c\cos\varphi}{1 + \sin\varphi} \leq 0 \quad \text{and} \quad \sqrt{s_{xx}^2 + s_{xy}^2} - \sigma_m - \frac{2c\cos\varphi}{1 - \sin\varphi} \leq 0. \tag{A.5}$$

Accordingly, three constraint conditions represented by three cones are used within SOCP (see Fig. 18). Each cone is formulated by means of its own stress tensor, i.e., $\boldsymbol{\sigma}^I$, $\boldsymbol{\sigma}^{II}$, and $\boldsymbol{\sigma}^{III}$ for Cone I, Cone II, and Cone III, respectively, giving three stress tensors for each material point. Finally, a

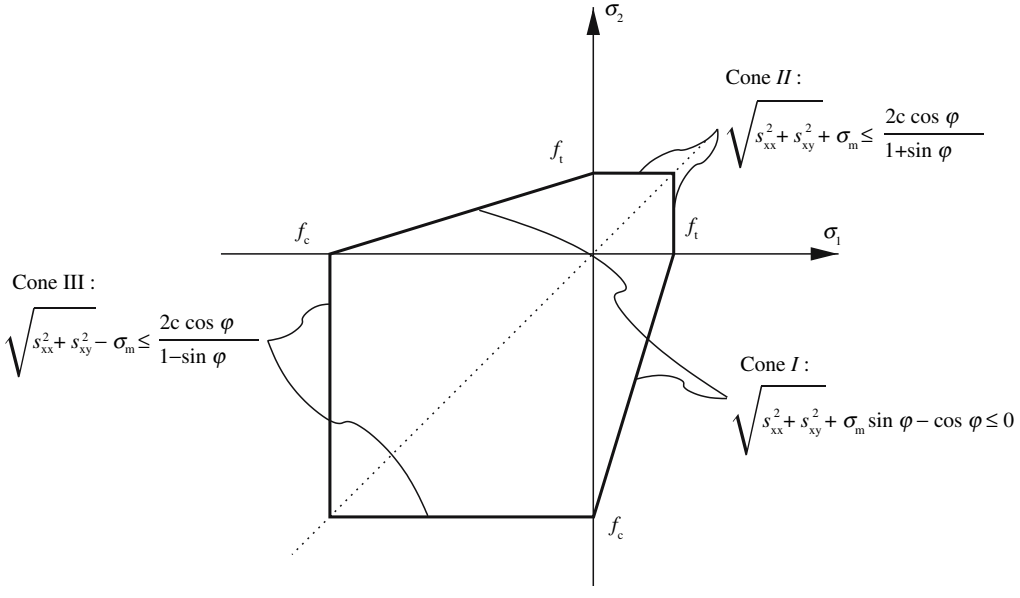

Fig. 18. Mohr–Coulomb failure surface for plane-stress situation and corresponding SOCP formulation (σ_1, σ_2: principle stresses)

unique solution for the stress tensor is enforced by additional equality constraints. The quantities for the respective cone formulation are given by

$$\text{Cone } I: \quad z^{I} = c\cos\varphi - \sin\varphi\sigma_m^{I}, \tag{A.6}$$

$$\text{Cone } II: \quad z^{II} = \frac{2c\cos\varphi}{1+\sin\varphi} - \sigma_m^{II}, \tag{A.7}$$

$$\text{Cone } III: \quad z^{III} = \frac{2c\cos\varphi}{1-\sin\varphi} + \sigma_m^{III}, \tag{A.8}$$

and $\mathbf{L}$, $\mathbf{y}$, and $\mathbf{q}_\sigma$ according to Eq. (A.4), with $\mathbf{q}_\sigma^{I} = \left\lfloor s_{xx}^{I}, s_{xy}^{I} \right\rfloor^T$, $\mathbf{q}_\sigma^{II} = \left\lfloor s_{xx}^{II}, s_{xy}^{II} \right\rfloor^T$ and $\mathbf{q}_\sigma^{III} = \left\lfloor s_{xx}^{III}, s_{xy}^{III} \right\rfloor^T$.

References

[1] Aigner, E., Lackner, R., Pichler, Ch.: "Bottom–up" multiscale modeling of viscoelastic properties of asphalt. Conf. Proc. Adv. Charact. Pavement Soil Engng. Mater. **1**, 123–135 (2007)

[2] Lackner, R., Mang, H.: Mehrskalenmodelle für die Berechnung von Flächentragwerken [Multiscale models for the analysis of shell structures]. Ernst & Sohn, Betonkalender 2007. In German, Band **2**, 19–65

[3] Lemarchand, E., Ulm, F.J., Dormieux, L.: Effect of inclusions on friction coefficient of highly filled composite materials. J. Engng. Mech. **128**(8), 876–884 (2002)

[4] Barthèlèmy, J.F., Dormieux, L.: A micromechanical approach to the strength criterion of Drucker–Prager materials reinforced by rigid inclusions. Int. J. Numer. Anal. Methods Geomech. **28**, 565–582 (2004)

[5] Heukamp, F.H., Lemarchand, E., Ulm, F.J.: The effect of interfacial properties on the cohesion of highly filled composite materials. Int. J. Solids Struct. **42**, 287–305 (2005)

[6] Zouain, N., Herskovits, J., Borges, L.A., Feijoo, R.A.: An iterative algorithm for limit analysis with non-linear yield functions. Int. J. Solids Struct. **30**(10), 1397–1417 (1993)

[7] Krabbenhoft, K., Lyamin, A.V., Hjiaj, M., Sloan, S.W.: A new discontinuous upper bound limit analysis formulation. Int. J. Numer. Methods Engng. **63**(7), 1069–1088 (2005)

[8] Makrodimopoulos, A., Martin, C.M.: Lower bound limit analysis of cohesive-frictional materials using second-order cone programming. Int. J. Numer. Methods Engng. **66**(4), 604–634 (2006)

[9] Lyamin, A.V., Sloan, S.W.: Upper bound limit analysis using linear finite elements and nonlinear programming. Int. J. Numer. Anal. Methods Geomech. **26**, 181–216 (2002)

[10] Lyamin, A.V., Sloan, S.W.: Lower bound limit analysis using non-linear programming. Int. J. Numer. Methods Engng. **55**, 573–611 (2002)

[11] Krabbenhoft, K., Damkilde, L.: A general non-linear optimization algorithm for lower bound limit analysis. Int. J. Numer. Methods Engng. **56**, 165–184 (2003)

[12] Gondzio, J.: HOPDM (version 2.12) – a fast LP solver based on a primal-dual interior point method. Eur. J. Oper. Res. **85**, 221–225 (1995)

[13] Abbo, A.J., Sloan, S.W.: A smoothed hyperbolic approximation to the Mohr–Coulomb yield criterion. Comput. Struct. **54**, 427–441 (1995)

[14] Makrodimopoulos, A., Bisbos, C.: Shakedown analysis of plane stress problems via SOCP. In: Staat, M., Heitzer, M. (eds.) Numerical Methods for Limit and Shakedown Analysis, pp. 185–216. John von Neumann Institute for Computing (NIC) (2003)

[15] Ciria, H., Peraire, J.: Computation of upper and lower bounds in limit analysis using second-order cone programming and mesh adaptivity. In: 9th ASCE Specialty Conference on Probabilistic Mechanics and Structural Reliability (2004)

[16] Makrodimopoulos, A.: Computational formulation of shakedown analysis as a conic quadratic optimization problem. Mech. Res. Commun. **33**, 72–83 (2006)

[17] Andersen, E.D., Roos, C., Terlaky, T.: On implementing a primal-dual interior-point method for conic quadratic optimization. Math. Program. Ser. B **95**, 249–277 (2003)

[18] MOSEK ApS (2006) The MOSEK optimization tools version 4.0 (revision 35). In: User's manual and reference. http://www.mosek.co. Cited 2006

[19] Makrodimopoulos, A., Martin, C.M.: Upper bound limit analysis using discontinuous quadratic displacement fields. Commun. Numer. Methods Engng. (2007) (in print)